Case Studies in Thermal Engineering 43 (2023) 102813

Contents lists available at ScienceDirect

Case Studies in Thermal Engineering

journal homepage: www.elsevier.com/locate/csite

Optimal design of thermal control system for space optical remote sensor based on NSGA-II and opto-mechanical-thermal integration analysis

Zhipeng Yuan [a,b], Liheng Chen [a,c,*], Hasiaoqier Han [a,c], Limin Ren [a,b], Shuai Liu [a,b], Renxin Wang [a,b]

[a] Changchun Institute of Optics, Fine Mechanics and Physics, Chinese Academy of Sciences, Changchun, 130033, China
[b] University of Chinese Academy of Sciences, Beijing, 10049, China
[c] Center of Materials Science and Optoelectronics Engineering, University of Chinese Academy of Sciences, Beijing, 100049, China

ARTICLE INFO

Handling Editor: Huihe Qiu

Keywords:
Space optical remote sensor
Thermal control system
Opto-mechanical-thermal integration
Surrogate model
Multi-objective optimization (MOO)
Non-dominated sorting genetic algorithm II

ABSTRACT

The thermal control system (TCS) is a key technology for ensuring good imaging quality of a space optical remote sensor (SORS) in orbit, and its research is of practical significance. In this paper, a multidisciplinary optimization method was proposed for the TCS of a SORS. A particle-swarm-optimized back-propagation neural network was used as the surrogate model to reduce the computational cost of the opto-mechanical-thermal integrated simulation model. Subsequently, the mean and variance of the modulation transfer function (MTF) of 12 fields of view of the SORS at the Nyquist frequency were considered as objective functions, multi-objective optimization of the design parameters of the TCS was performed using the non-dominated sorting genetic algorithm II (NSGA-II), and the Pareto front composed of a series of Pareto solutions was obtained. A compromise solution was selected as the optimal TCS design. The results showed that, upon comparison with the initial design, the optimal design scheme increased the mean of the MTFs of the SORS by 34.4%, reduced the variance by 31.3%, and significantly improved the comprehensive optical performance of the SORS.

Nomenclature

A_d	area of node d (m^2)
A_h	area of node h (m^2)
$B_{d,h}$	Gebhardt coefficient
c	specific heat capacity (J/kg•K)
D	thermal conductivity (W/m•K)
$D_{d,h}$	thermal conductivity between node d and node h (W/m•K)
E_a	average albedo of the earth's surface to the sun (W/m^2)
E_e	average infrared radiation intensity on earth's surface (W/m^2)
m	mass (kg)

* Corresponding author. Changchun Institute of Optics, Fine Mechanics and Physics, Chinese Academy of Sciences, Changchun, 130033, China.
E-mail address: chenliheng3@163.com (L. Chen).

https://doi.org/10.1016/j.csite.2023.102813
Received 15 July 2022; Received in revised form 9 February 2023; Accepted 11 February 2023
Available online 13 February 2023

Q_s	heat flow outside the space absorbed by the camera (W)
Q_{sh}	heat flow outside the space absorbed by node h (W)
Q_p	thermal power consumption of the camera (W)
Q_{ph}	thermal power consumption of node h (W)
Q_c	internal energy increment of the camera (J)
Q_{ch}	internal energy increment of node h (J)
S	solar constant (W/m^2)
T	temperature of the camera (K)
T_d	temperature of node d (K)
T_h	temperature of node h (K)

Greek symbols

ε	infrared emissivity
ε_d	infrared emissivity of node d
ε_h	infrared emissivity of node h
α_s	solar absorptivity
α_{sh}	solar absorptivity of node h
σ	Stefan-Boltzmann constant, 5.67×10^{-8} (W/m^2•K^4)
$\varphi_{1,h}$	viewing angle coefficient of node h relative to the direct solar heat flow
$\varphi_{2,h}$	viewing angle coefficient of node h relative to the earth's average albedo heat flow
$\varphi_{3,h}$	viewing angle coefficient of node h relative to the earth's average infrared radiation heat flow
τ	time (s)
β	angle between the sun vector and the orbital plane

Abbreviations

SORS	space optical remote sensor
TCS	thermal control system
NSGA-II	non-dominated sorting genetic algorithm II
MOO	multi-objective optimization
PSO	particle swarm optimization
BPNN	back propagation neural network
MTF	modulation transfer function

1. Introduction

The development of space optical remote sensor (SORS) technology has made the exploration of the universe increasingly convenient for humans. However, the harsh space environment poses major challenges. A typical SORS exchanges heat with the sun's direct heat flow, the earth's albedo heat flow, the earth's infrared heat flow, and the cold and dark space when it works in orbit; it is further affected by the internal heat source, thus resulting in different temperatures in different parts of the SORS. The temperature gradient of the optical system causes deformation of the mirror and support structure, which in turn, reduces the image quality [1]. When the temperature of a SORS is maintained within a reasonable range, good optical performance can be obtained. The thermal control system (TCS) is a type of temperature control system commonly used in spacecraft, which combines passive measures, such as multi-layer thermal insulation assembly (MLI), thermal insulation pads, thermal conductive materials, and thermal control coatings, and active measures, such as pasting heating sheets, and temperature sensors. The system is based on passive measures supplemented by active measures and has high reliability. Therefore, many researchers have investigated TCS of different SORSs to ensure their optical performance in stabilizing temperature within a reasonable range. Jaekel et al. [2] discussed a TCS for a faint object camera (FOC) which guarantees strict image stabilization based on active and passive thermal control measures. Zhang et al. [3] evaluated the TCS of the hard X-ray modulation telescope (HXMT), which is a large scientific instrument developed in China. Through numerical simulation, they obtained the relationship between the temperature of the HXMT, the change in external heat flow, and the thickness of the MLI. Shaughnessy et al. [4] introduced a detailed design and testing process of the TCS of the mid-infrared instrument (MIRI), which is a scientific instrument of the James Webb space telescope (JWST) observatory, to ensure that it is the coldest instrument at the observatory. Morgante et al. [5,6] developed a TCS of the exoplanet characterization observatory (EChO), which utilized three main cooling methods to maintain the required observation temperature of various instruments in the EChO. Li et al. [7,8] introduced a TCS of a solar X-ray and extreme ultraviolet imager that could effectively reduce the received direct solar heat flow, ensure extremely low operating temperature of the CCD, and maintain the temperature difference between the CCD and surrounding components at 80 °C. Additionally, extensive research has been conducted to improve the temperature control efficiency of a TCS. Escobar et al. [9] explored an automatic design method for satellite TCS based on the genetic algorithm and used finite element simulation to evaluate possible schemes. Yang et al. [10] introduced a back propagation (BP) neural network as a surrogate model and performed global sensitivity analysis to determine the parameters in the TCS that had a significant impact on the spectrometer frame temperature. They reported

that this method would play a significant role in guiding the design of TCS for space cameras. Zhang et al. [11] applied the Taguchi method and integrated thermo-optical analysis to optimize and experimentally verify the TCS of a space camera. Cataldo et al. [12] developed a fully automated model validation method with significantly reduced cycle times and successfully applied it to several thermal management subsystems of the JWST. Galski et al. [13] and Muraoka et al. [14] introduced a TCS optimization strategy based on the generalized extremal optimization (GEO) algorithm, which was successfully applied to the TCS optimization design of the Brazilian multi-mission platform (PMM).

In the aforementioned design and optimization studies of the TCS, the goal was to maintain the temperature of optical elements and other important components within the temperature specification, thereby guaranteeing the optical performance of the SORS. To explore the influence of temperature on the optical performance of the SORS more intuitively, an integrated analysis was performed in the initial stages of its design. For example, the integrated science instrument module (ISIM) of the JWST [15], the subarcsecond telescope and balloon experiment (STABLE) platform [16], the field-widened Michelson interferometer of the high spectral resolution lidar (HSRL) project [17], and the laser transmitter for the ICESat-2 Mission [18] have performed extensive structural-thermal-optical-performance (STOP) analysis to predict the optical performance of the device in orbit.

Generally, the TCS of SORS is designed by thermal engineers according to the temperature control objectives and completed by continuous iterative optimization. However, parameter changes in TCS may cause uncertainty in the optical performance of SORS, and the given design may not guarantee the optimal optical performance of SORS [19]. Therefore, a multi-objective optimization (MOO) method was considered in this paper, which accounted for not only the size of the MTF at the Nyquist frequency for different fields of view of the SORS but also the difference in the MTF, such that the SORS could obtain good optical performance in orbit.

The non-dominated sorting genetic algorithm II (NSGA-II) is a classic MOO algorithm proposed by Deb et al. [20] in 2002. It adopts the hierarchical fast non-dominated sorting method and elite strategy, reduces the complexity of the algorithm and improves its efficiency. NSGA-II has been applied in many engineering fields. Yang et al. [21] applied NSGA-II to optimize the design parameters that have a significant influence on the plate-fin heat exchanger with serrated fins and determine the optimal design. Arora et al. [22] used NSGA-II to realize the optimal design of a thermoelectric generator (TEG) and simultaneously improved its output power, thermal efficiency and ecological function of TEG. Zhang et al. [23] adopted different optimization strategies according to the flight altitude of a hybrid airship and reduced its total mass and energy cost through NSGA-II. Lee et al. [24] proposed a robust design optimization (RDO) method for TEG systems. They used the Kriging model to establish a surrogate model of the TEG net power output and searched for a compromise solution based on NSGA-II, thereby reducing the sensitivity of the TEG net power output to parameter uncertainty.

Therefore, the primary goal of this study was to introduce NSGA-II into the opto-mechanical-thermal integration analysis aimed at optical performance, to explore the optimal design of the TCS of SORS during on-orbit operation. The design of TCS is crucial because it enables SORS to obtain stable optical performance by regulating its temperature in the complex space environment. During the optimization process, the mean and variance of the MTFs at the Nyquist frequency for the 12 fields of view of the SORS were included in the objective function. In order to save the computation time and resources of the MOO process, an approximation model between the TCS design parameters and the optical performance of the SORS based on a surrogate model was used in this paper.

The remainder of this paper is organized as follows. In section 2, the optimization framework of TCS, including TCS parameter selection, opto-mechanical-thermal integrated simulation analysis, and surrogate model modeling are described. Section 3 includes the introductions of the MOO process and the NSGA-II method. In section 4, the results are analyzed and discussed. Finally, the paper is summarized in section 5.

2. Optimization framework

Fig. 1 shows the MOO framework of TCS that included 4 steps: 1) parameter selection, 2) opto-mechanical-thermal integration simulation analysis, 3) surrogate model modeling, and 4) execution of the MOO process. Sections 2.1 and 2.2 include the selection of TCS design parameters and analysis of the opto-mechanical-thermal integration simulation. Section 2.3 consists of the theoretical

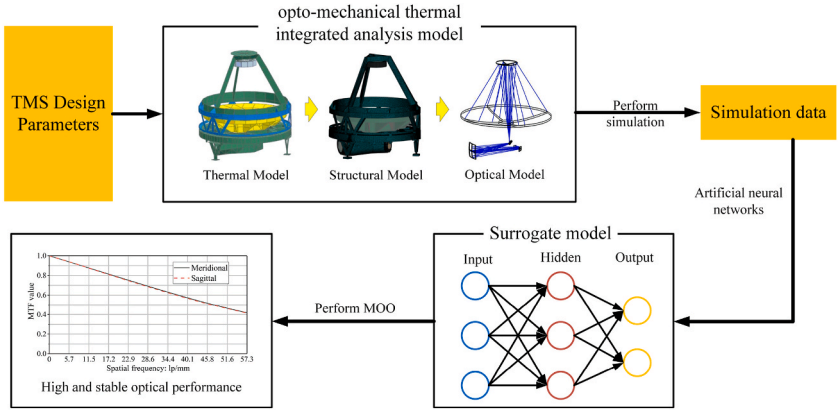

Fig. 1. Schematic diagram of the optimization framework of TCS.

background and validation of the adopted surrogate model. Section 3 comprises the detailed introduction of the MOO process based on NSGA-II.

2.1. Selection of TCS optimization parameters

In this paper, we used a certain SORS model, and the partial design of its TCS is shown in Fig. 2. Generally, MLI is used to separate a SORS from the external environment and provide thermal insulation. The heat-conducting cable conducts the heat generated by the internal heat source to the heat dissipation surface. Heaters are used in conjunction with sensors to compensate for the heat loss of certain components. Occasionally, it is also necessary to change the surface properties of objects through thermal control coatings.

Typically, temperature field changes cause thermal deformation of the optical elements and supporting structures of SORS, which in turn, affect the optical performance of the entire system. Therefore, to determine the TCS design parameters that affect optical performance, the heat transfer model of the SORS was analyzed. According to the law of conservation of energy, the heat balance equation of any node h is established, as follows:

$$Q_{sh} + Q_{ph} + \sum_{d=1}^{p} B_{d,h} A_d \varepsilon_d \sigma T_d^4 + \sum_{d=1}^{q} D_{d,h}(T_h - T_d) = Q_{ch} + A_h \varepsilon_h \sigma T_h^4 \tag{1}$$

where Q_{sh} is the heat flow absorbed by node h from the external space, and Q_{ch} is the increment in internal energy of node h, which can be expressed as Eqs. (2) and (3), respectively.

$$Q_{sh} = \left(\alpha_{sh} S \varphi_{1,h} + \alpha_{sh} E_a \varphi_{2,h} + \varepsilon_h E_e \varphi_{3,h}\right) A_h \tag{2}$$

$$Q_{ch} = (mc)_h \frac{dT_h}{d\tau} \tag{3}$$

In Eq. (1), Q_{ph} represents the heat generated by node h. $\sum_{d=1}^{p} B_{d,h} A_d \varepsilon_d \sigma T_d^4$ represents the radiant heat absorbed by node h from other nodes, and $B_{d,h}$ is the Gebhardt coefficient. $\sum_{d=1}^{q} D_{d,h}(T_h - T_d)$ is the heat exchanged between node h and the connected node d, and $D_{d,h}$ is the thermal conductivity between node h and node d. $A_h \varepsilon_h \sigma T_h^4$ represents the heat radiated from node h. In Eq. (2), α_{sh} and ε_h represent the solar absorptivity and emissivity of the node h surface, respectively. S, E_a, and E_e represent the solar constant, average albedo intensity of the earth's surface to the sun, and average infrared radiation intensity of the earth's surface, respectively; these parameters depend on the orbital height. $\varphi_{\lambda,h}(\lambda = 1, 2, 3)$ represents the viewing angle coefficients of node h relative to the direct solar heat flow, the earth's average albedo heat flow, and the earth's average infrared radiation heat flow, respectively, which are generally determined by the orbital position of the camera, flight attitude, and structure of the camera. Therefore, an implicit equation representing the temperature of the SORS can be obtained, as follows:

$$T = f\left(Q_p, \alpha_s, \varepsilon, B, D, \sigma, S, E_a, E_e, \varphi, mc, \ldots\right) \tag{4}$$

Assuming that the structure and mission of the SORS considered in this paper have been determined, S, E_a, E_e, and φ are non-adjustable parameters. Q_p is the fixed internal heat source during the orbital operation of the SORS. σ is the Stefan-Boltzmann constant, that is 5.67×10^{-8} $W/(m^2 \cdot K^4)$. α_s, ε, B, D and mc are thermophysical properties determined by the material and surface state of the object and are adjustable parameters. However, mc represents the heat capacity of the object, which does not affect the equilibrium temperature and only affects the time taken to attain equilibrium.

Considering that the SORS works in a vacuum environment, only the TCS design parameters related to radiation and conduction were considered for parameter selection. Therefore, based on the analysis results combined with our experience in engineering design, the main adjustable parameters that affected the temperature of the optical elements and support structures were selected. Due to the unique requirements of the reflective surface of the optical elements, only the emissivity of the back of the optical elements, and the contact heat transfer coefficient of the mounting surface were selected as design parameters. Additionally, the emissivity of components capable of radiative heat exchange with the optical elements and support structures were considered. The contact thermal

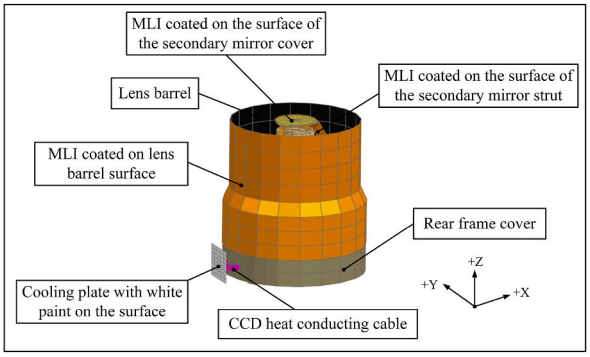

Fig. 2. Part of the design of TCS.

resistance between the support structures and other parts was another main factor affecting its temperature. Table 1 lists the selected 21 TCS design parameters and their corresponding description.

2.2. Simulation analysis of opto-mechanical-thermal integration

To describe the relationship between the TCS design parameters and optical performance of the system, an opto-mechanical-thermal integration simulation analysis was performed in this paper [25,26]. 1) First, according to the structural model of the SORS and the design scheme of the TCS, the thermal analysis model of the SORS was established based on the NX Space System Thermal module. Subsequently, the temperature field of the SORS was obtained by solving the established thermal analysis model. 2) The temperature field was mapped component-to-component on the structural analysis model of the SORS established in NX Nastran. Thereafter, thermal deformation analysis was performed to obtain the rigid body displacement of the optical elements and the nodal deformation of its surface. 3) Since the Zernike polynomial [27] has the advantages of being orthogonal to the unit circle and easily corresponding to optical aberrations, it can fit the surface shape of the deformed optical element well, and it is generally used as the data conversion tool for optical and structural analysis. 4) Finally, the original optical model in Zemax was corrected using the fitted Zernike polynomial coefficients, and the optical performance index of the SORS was obtained through optical analysis.

In this paper, an extreme condition of a SORS on-orbit operation was considered, as summarized in Table 2. The flight attitude of the SORS changed periodically with the roll angle of the satellite from 0° to ±15° in one orbital period, and the positive direction of the roll angle was defined as the rotation from $+Z$ to $+Y$. $\beta = -66°$ implied that the angle between the sun vector and orbital plane was $-66°$. The thermophysical properties of the MLI surface and heat dissipation surface coating were the solar absorption emission ratios $\alpha_s/\varepsilon = 0.3/0.84$ and $\alpha_s/\varepsilon = 0.35/0.86$, respectively, at the end of their life. The solar constant S was considered as the solar radiation intensity of 1412 W/m^2 at the winter solstice. The maximum temperature of the bottom cold plate was 26 °C. The temperatures of other single machines around the SORS were considered as the maximum values of their temperature control targets.

To ensure the spatial uniformity of the training data set, we adopted the Latin hypercube sampling method to sample the 21 design parameters listed in Table 1 within their value ranges. Subsequently, through the above-analyzed opto-mechanical-thermal integration simulation process, the imaging behavior of the SORS was simulated for changes in TCS design parameters under the extreme working condition, and the MTFs of 12 fields of view at all sampling points were obtained. A total of 1875 datasets with 21 inputs and 12 outputs were obtained, which were divided into training and test sets for the training and testing of the surrogate model.

2.3. Surrogate model

According to the analysis in Section 2.2, the simulation analysis of opto-mechanical-thermal integration is a complex and time-consuming process, and is computationally expensive to use the simulation model to find the optimal solution in the optimization process. Therefore, to perform MOO quickly and efficiently, surrogate models (also called metamodels) were used to replace the expensive simulation processes. The goal was to construct the mapping relationship as accurately as possible using limited and expensive simulation data and predict the response value of the system at the new point. Surrogate models [28,29] commonly used in engineering design and optimization include the polynomial response surface method, Kriging method, support vector machine, and artificial neural networks. Kim et al. [30] developed a surrogate model using artificial neural networks to rapidly predict the behavior of time-dependent storm surges. Dong et al. [31] used the L1 optimization method to adjust the structure of a back propagation neural network (BPNN), obtained the most compact and applicable network mapping structure and applied it to antenna design optimization problem.

Table 1
Description of 21 TCS design parameters.

Parameter	Description	Range
X_1	Contact heat transfer coefficient between secondary mirror and mounting frame ($W/(m^2 \cdot K)$)	100 ~ 2000
X_2	Contact heat transfer coefficient between primary mirror and support sleeve ($W/(m^2 \cdot K)$)	100 ~ 2000
X_3	Contact heat transfer coefficient between third mirror and mounting frame ($W/(m^2 \cdot K)$)	100 ~ 2000
X_4	Surface emissivity on the back of the secondary mirror	0.1 ~ 0.9
X_5	Surface emissivity on the back of the primary mirror	0.1 ~ 0.9
X_6	Surface emissivity on the back of the third mirror	0.1 ~ 0.9
X_7	Surface emissivity at the bottom of the secondary mirror holder	0.1 ~ 0.9
X_8	Surface emissivity of camera mount	0.1 ~ 0.9
X_9	Emissivity of the inner surface of the secondary mirror heating cover	0.1 ~ 0.9
X_{10}	Emissivity of the outer surface of the third mirror cover	0.1 ~ 0.9
X_{11}	Emissivity of the inner surface of the rear frame cover	0.1 ~ 0.9
X_{12}	Emissivity of the inner surface of the bottom of the lens barrel	0.1 ~ 0.9
X_{13}	Surface emissivity on top of radiant heating plate	0.1 ~ 0.9
X_{14}	Surface emissivity on bottom of radiant heating plate	0.1 ~ 0.9
X_{15}	Thermal resistance between radiant heating plate and rear frame (K/W)	0.01 ~ 50
X_{16}	Thermal resistance between camera mount and mounting point (K/W)	0.01 ~ 50
X_{17}	Thermal resistance between electrical box 1 and rear frame (K/W)	0.01 ~ 100
X_{18}	Thermal resistance between electrical box 2 and rear frame (K/W)	0.01 ~ 100
X_{19}	Thermal resistance between focusing mechanism and rear frame (K/W)	0.01 ~ 50
X_{20}	Equivalent heat transfer coefficient of MLI of secondary mirror strut ($W/(m^2 \cdot K)$)	0.02 ~ 0.2
X_{21}	Equivalent heat transfer coefficient of MLI of secondary mirror cover ($W/(m^2 \cdot K)$)	0.02 ~ 0.2

Table 2
Parameter description under the extreme working condition.

Item	Description
Flight attitude	The roll angle varies periodically from 0° to ±15°
β	− 66°
Surface properties of MLI	$\alpha_s/\varepsilon = 0.3/0.84$
Coating properties of heat dissipating surface	$\alpha_s/\varepsilon = 0.35/0.86$
Solar constant S	1412 W/m^2
Temperature of bottom cold plate	26 °C

2.3.1. Back propagation neural network

A back propagation neural network [32] (BPNN) is a multi-layer feedforward neural network that uses an error back-propagation algorithm to correct network weights and thresholds. It has strong nonlinear fitting ability and can approximate the functional relationship between the input and output with arbitrary precision.

Fig. 3 shows the topology of a BPNN, including the input layer, hidden layer, and output layer, which can have multiple hidden layers. Information is transferred between layers through weights and biases. Generally, the training of a BPNN is divided into two steps: forward transfer of information to obtain the predicted value and backward transfer of error to correct the connection weights and biases.

In the information forward transfer process, the model prediction value can be expressed as follows:

$$\widehat{\boldsymbol{Y}} = z_2\left(\boldsymbol{V}^T z_1\left(\boldsymbol{W}^T\boldsymbol{X} + \mathbf{b}_1\right) + \mathbf{b}_2\right) \tag{5}$$

where $z_1(\cdot)$ and $z_2(\cdot)$ are activation functions. $\boldsymbol{W}$ and $\mathbf{b_1}$ are the weight matrix and bias vector of the input layer and the hidden layer, respectively; $\boldsymbol{V}$ and $\mathbf{b_2}$ are the weight matrix and bias vector of the hidden layer and the output layer, respectively. $\boldsymbol{X} = [\mathbf{x}_1, \mathbf{x}_2, \cdots, \mathbf{x}_n] \in \boldsymbol{R}^m$ represents n sample points, and $\widehat{\boldsymbol{Y}} = [\widehat{\mathbf{y}}_1, \widehat{\mathbf{y}}_2, \cdots, \widehat{\mathbf{y}}_n] \in \boldsymbol{R}^{mn}$ represents n predicted responses of the model. For a model with n sets of training data and m-dimensional output, the loss function E can be expressed as follows:

$$E = \frac{1}{n}\frac{1}{m}\sum_{i}^{n}\sum_{j}^{m}\left(\mathrm{y}_{ij} - \widehat{\mathrm{y}}_{ij}\right)^2 \tag{6}$$

where y is the true value, and $\widehat{\mathrm{y}}$ is the predicted value.

In the error backward transfer process, the gradient of the loss function with respect to the weights and biases was first obtained, and then, the weights and biases were updated in the negative direction of the gradient. The update process can be expressed as follows:

$$\boldsymbol{V}^{(k)} = \boldsymbol{V}^{(k-1)} - \eta\frac{\partial E}{\partial \boldsymbol{V}^{(k-1)}} \tag{7}$$

$$\boldsymbol{b}_2^{(k)} = \boldsymbol{b}_2^{(k-1)} - \eta\frac{\partial E}{\partial \boldsymbol{b}_2^{(k-1)}} \tag{8}$$

$$\boldsymbol{W}^{(k)} = \boldsymbol{W}^{(k-1)} - \eta\frac{\partial E}{\partial \boldsymbol{W}^{(k-1)}} \tag{9}$$

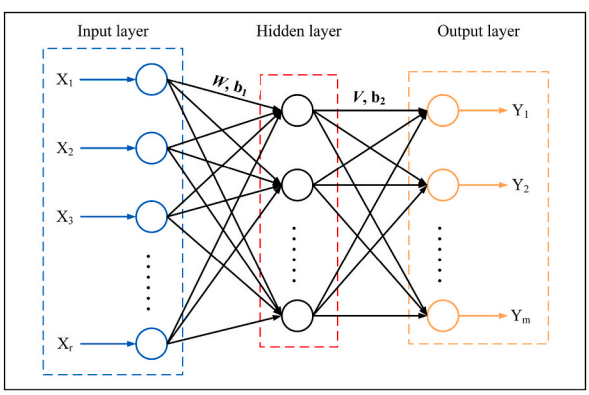

Fig. 3. Structure of BPNN.

$$\boldsymbol{b}_1^{(k)} = \boldsymbol{b}_1^{(k-1)} - \eta \frac{\partial E}{\partial \boldsymbol{b}_1^{(k-1)}} \tag{10}$$

where η is the learning rate, and k and $k-1$ are the kth update and the $(k-1)$th update, respectively. The BPNN was trained by repeating these two processes continuously until the error met the training objective. Thereafter, the generalization ability of the network was tested using the test set, and the trained network was applied to the next prediction task.

2.3.2. Particle swarm optimization

The particle swarm optimization (PSO) algorithm is a random search algorithm proposed by Kennedy and Eberhart, inspired by the foraging behavior of birds [33]. In the process of simulating the foraging behavior of birds, the solution space of the problem is assumed to be the flight space of the birds, and each possible solution is regarded as a bird in the search space, which is abstracted as a particle without mass and volume. Each particle determines the search direction and distance according to its own speed and evaluates the quality of the particle by calculating the fitness value. Typically, the dimension of the solution space is determined by the number of variables L to be optimized, and the velocity and position of the particles are updated as follows:

$$\boldsymbol{v}_l^{t+1} = \boldsymbol{v}_l^t + c_1 r_1^t \left(\boldsymbol{pbest}_l^t - \boldsymbol{x}_l^t\right) + c_2 r_2^t \left(\boldsymbol{gbest}^t - \boldsymbol{x}_l^t\right) \tag{11}$$

$$\boldsymbol{x}_l^{t+1} = \boldsymbol{x}_l^t + \boldsymbol{v}_l^{t+1} \tag{12}$$

where $l = 1, 2, \cdots, M$, M is the population size. t and $t+1$ represent the tth iteration and the $(t+1)$th iteration, respectively. c_1 and c_2 are non-negative constants called acceleration factors. r_1 and r_2 are random numbers in $[0, 1]$. $\boldsymbol{v}_l = (v_{l1}, v_{l2}, \cdots, v_{lD})$ represents the flight speed of the lth particle. $\boldsymbol{x}_l = (x_{l1}, x_{l2}, \cdots, x_{lD})$ represents the position of the lth particle. $\boldsymbol{pbest}_l$ represents the position where the lth particle has the best fitness value among the positions it has experienced and is called the individual extreme value, which can be expressed by the following equation [34]:

$$\boldsymbol{pbest}_l^{t+1} = \begin{cases} \boldsymbol{x}_l^{t+1}, & g\left(\boldsymbol{x}_l^{t+1}\right) \geq g\left(\boldsymbol{pbest}_l^t\right) \\ \boldsymbol{pbest}_l^t, & otherwise \end{cases} \tag{13}$$

where $g(\cdot)$ is the fitness function. $\boldsymbol{gbest}$ represents the position with the best fitness value among the positions searched by all particles and is called the group extremum, which can be expressed as follows:

$$\boldsymbol{gbest}^{t+1} = \underset{\boldsymbol{pbest}}{\operatorname{argmax}}\left(g\left(\boldsymbol{pbest}_l^{t+1}\right)\right) \tag{14}$$

Finally, in addition to the optimal individual, several sub-optimal individuals were obtained.

2.3.3. PSO-BPNN surrogate model modeling

In this subsection, a three-layer BP neural network is used to construct the mapping relationship between the TCS design parameters and the MTFs of the SORS. To obtain good learning ability and improve the prediction accuracy of the surrogate model, PSO was used to optimize the initial neuron connection weights and biases of BPNN. The number of variables to be optimized was expressed as follows:

$$L = Num_{in} \cdot Num_{hide} + Num_{hide} + Num_{out} \cdot Num_{hide} + Num_{out} \tag{15}$$

where Num_{in} represents the number of neurons in the input layer, which is equal to the number of design parameters of the TCS. Num_{hide} represents the number of neurons in the hidden layer. In this paper, 15 neurons were set in the hidden layer. Num_{out} represents the number of neurons in the output layer, which is equal to the number of MTFs of the SORS. Therefore, the total number of connection weights and biases of the BPNN was 522. The activation function plays a vital role in the training process of the PSO-BPNN. Generally, the sigmoid function is used as the activation function between the input layer and the hidden layer, as follows:

$$z_1(x) = \frac{1}{1 + e^{-x}} \tag{16}$$

The activation function between the hidden layer and the output layer was a linear function. 1675 sets of samples were randomly selected from the dataset obtained in Section 2.2 for training, and the remaining 200 sets of samples were used for testing. In this paper, the mean square error (MSE) and coefficient of determination (R^2) were used to evaluate the training accuracy and generalization ability of the PSO-BPNN surrogate model, as follows:

$$MSE = \frac{1}{N} \sum_{i=1}^{N} (y_i - \hat{y}_i)^2 \tag{17}$$

$$R^2 = 1 - \sum_{i=1}^{N} (y_i - \hat{y}_i)^2 \Big/ \sum_{i=1}^{N} (y_i - \bar{y})^2 \tag{18}$$

where N represents the number of sample points, and $\bar{y}$ represents the average value of the true value. The closer the MSE is to 0 and R^2

is to 1, the higher is the accuracy of the model.

3. Methodologies for TCS optimization

3.1. Multi-objective optimization

Multi-objective optimization (MOO) problems are involved in all aspects of production and life and have attracted the attention of several researchers. The study of such problems has important practical significance. Typically, the sub-objectives of MOO problems compete with each other. The optimal solution of a single objective can-not obtain the optimal system performance, and it does not exist to simultaneously obtain the optimal solution of multiple objectives. Therefore, the solution of the MOO problem is not unique, but a Pareto optimal solution set consisting of a set of Pareto solutions. Decision makers can choose a compromise solution according to the design requirements to optimize the system performance as much as possible.

In this paper, MOO was introduced into the parameter optimization design of the TCS. To ensure that the SORS had good optical performance while working in orbit, the mean value of the MTFs at the Nyquist frequency of different fields of view of the SORS was maximized, and the variance was minimized simultaneously. Table 1 lists the decision variables of the TCS optimization problem. Therefore, the MOO formula for the TCS design parameters is expressed as follows:

$$\begin{cases} \min\limits_{\mathbf{x}} \quad f_1(\mathbf{x}) = -\mu(\widehat{\boldsymbol{Y}}_{MTF}(\mathbf{x})) \\ \qquad f_2(\mathbf{x}) = \sigma^2(\widehat{\boldsymbol{Y}}_{MTF}(\mathbf{x})) \\ subject \quad to \quad \mathbf{lb} \le \mathbf{x} \le \mathbf{ub} \end{cases} \tag{19}$$

where $\mathbf{x}$ represents the vector of TCS design variables, and $\mathbf{lb}$ and $\mathbf{ub}$ are the lower and upper bounds of the design variables, respectively. $\widehat{\boldsymbol{Y}}_{MTF}$ represents the output vector of the PSO-BPNN surrogate model. μ represents the mean of the output vector, and σ^2 represents the variance of the output vector.

3.2. Non-dominated sorting genetic algorithm II

NSGA-II is a popular intelligent optimization algorithm. It is an improvement on NSGA owing to the introduction of non-dominated sorting, proposal of crowding degree and crowding degree comparison operators, and introduction of elite strategy that improves the operation speed and robustness of the algorithm [35]. Fig. 4 shows the selection process of NSGA-II, where $Gen(Gen \ge 2)$ represents the number of evolutions, P and Q represent the parent and offspring populations, respectively, and $\{F_1, F_2, F_3 \cdots\}$ represents the non-dominated sorted fronts.

As shown in Fig. 5, the principle of NSGA-II is as follows. First, a parent population of size N is randomly generated and sorted by the introduced non-dominated sorting algorithm to create multiple non-dominated sorted fronts. A single solution x^* dominates the other solutions if it has at least one objective better than the others and none of its objectives are worse than the others. Solutions not dominated by any other are called non-dominated solutions, also known as Pareto solutions. In the sorting process, first, all non-dominated solutions are identified from the population of size N and assigned to the first-level non-dominated front F_1, and the individuals in F_1 are removed from the population. Then, all non-dominated solutions are identified from the remaining population of size $N - F_1$ and assigned to the second-level non-dominated front F_2, and the individuals in F_2 are removed from the remaining population. This process is repeated until all individuals in the population are assigned to different non-dominated fronts. The non-dominated sorting algorithm greatly reduces computational complexity. The sorted parent population generates an offspring population of size N through the selection, cross, and mutation operations of the traditional genetic algorithm. Second, the parent and offspring populations are merged into a new population of size $2N$, and non-dominated sorting is performed. Meanwhile, the crowding degree and crowding distance of individuals in each non-dominated front are calculated, and N suitable individuals are selected to form a new parent population. Each evolution competes among $2N$ parent and offspring individuals. Finally, the above operations are repeated until the Pareto optimal front is obtained within a given convergence or stopping criterion

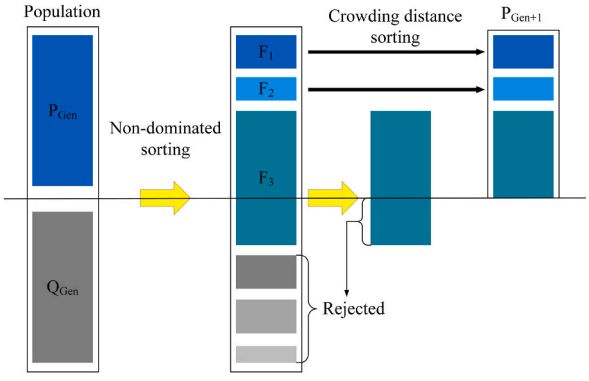

Fig. 4. Selection process of NSGA-II

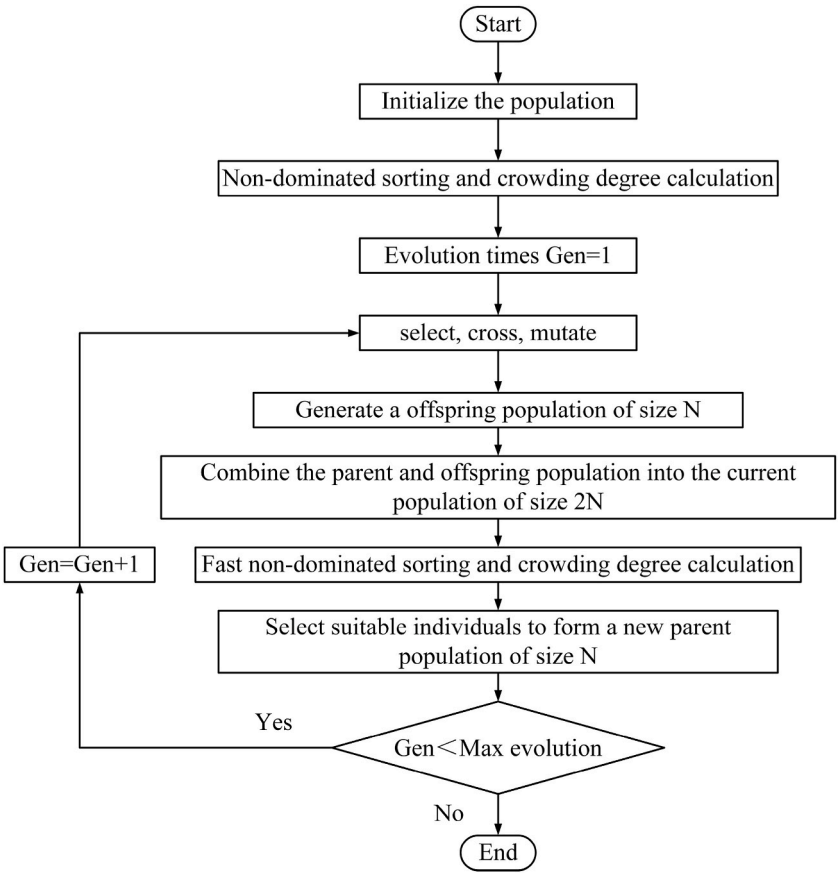

Fig. 5. Flowchart of NSGA-II

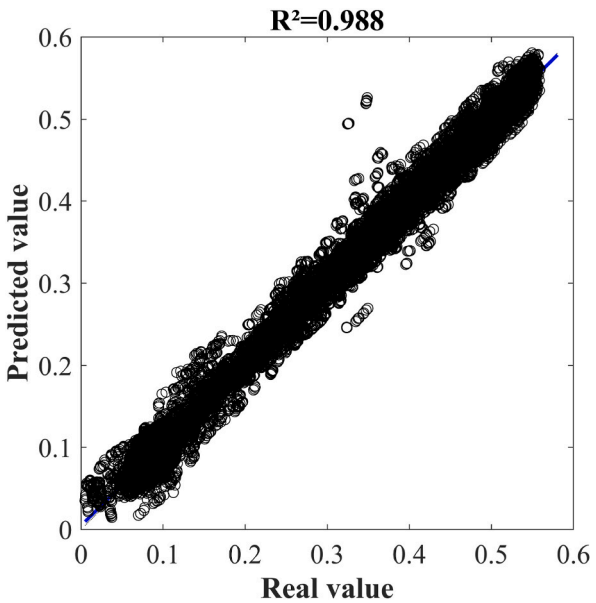

Fig. 6. Regression plot of predicted and true values on the training set.

4. Results and discussion

4.1. Analysis of modeling results of PSO-BPNN surrogate model

The global optimal individual obtained by PSO was used as the initial connection weight and bias of the BPNN, and thereafter, the BPNN was trained. Fig. 6 shows the regression plot of predicted and true values on the training set after iterative training, and the evaluation indicators MSE and R^2 of the surrogate model were obtained as 0.00033 and 0.988, respectively. The results showed that the PSO-BPNN surrogate model achieved a good learning effect and could accurately map the relationship between the input and output.

To evaluate the generalization ability of the PSO-BPNN surrogate model, 200 sets of samples were used for testing, and the evaluation indicators MSE and R^2 were obtained as 0.0006 and 0.981, respectively. Fig. 7 shows the regression plot of the predicted and true values on the test set.

It is worth noting that through the established PSO-BPNN surrogate model, the optical performance of SORS could be quickly obtained by only inputting the TCS design parameters, which solves the problem of the considerable time cost for completing an opto-mechanical-thermal integrated analysis.

4.2. Analysis of MOO results of TCS design parameters

In this section, the results of the MOO of TCS design parameters for the SORS using NSGA-II based on the PSO-BPNN surrogate model are presented. The number of iterations was set to 1000 and the population size was set to 100 during optimization. The optimization program based on the surrogate model took 0.0193s for each iteration, which was clearly advantageous compared to the optimization based on the opto-mechanical-thermal integration simulation, which took tens of minutes for each iteration.

Fig. 8 shows the Pareto front obtained from MOO. The figure shows that, with an increase in μ, σ^2 increased gradually, which indicated that, while the optical performance was improved, the differences in the optical performance of different fields of view increased. Conversely, as σ^2 gradually decreased, μ decreased, indicating that the optical performance decreased, while the differences in the optical performance of different fields of view decreased.

A multi-objective optimization function improves μ with a suitable σ^2. In this paper, a compromise solution was chosen based on the principle of obtaining a higher mean value of MTFs while ensuring a lower variance of MTFs. Table 3 lists the means and variances of the MTFs at the Nyquist frequency for the 12 fields of view of SORS for the three optimized solutions. Under the optimization scheme targeting the mean of MTFs, the maximum value of μ was 0.60692, and the maximum value of σ^2 was 1.649×10^{-4}. Under the optimization scheme targeting the variance of MTFs, the minimum value of μ was 0.02324 and the minimum value of σ^2 was 0.274×10^{-4}. Due to the contradiction between μ and σ^2 in optimization, if one of the functions was used as the optimization objective, the resulting design could not satisfy the other objective. Contrarily, a compromise solution could better meet the design requirements of the system. Therefore, a compromise solution is considered as the optimal design of the TCS of the SORS. In addition, it can be seen from Table 3 that the maximum relative error between the predicted and simulated values of μ and σ^2 is 9.5%, less than 10%, which meets the requirements of engineering applications and further verifies the prediction reliability of the PSO-BPNN surrogate model. Table 4 lists the decision variables of the initial design scheme and the optimal design scheme, and the specific parameter descriptions are listed in Table 1.

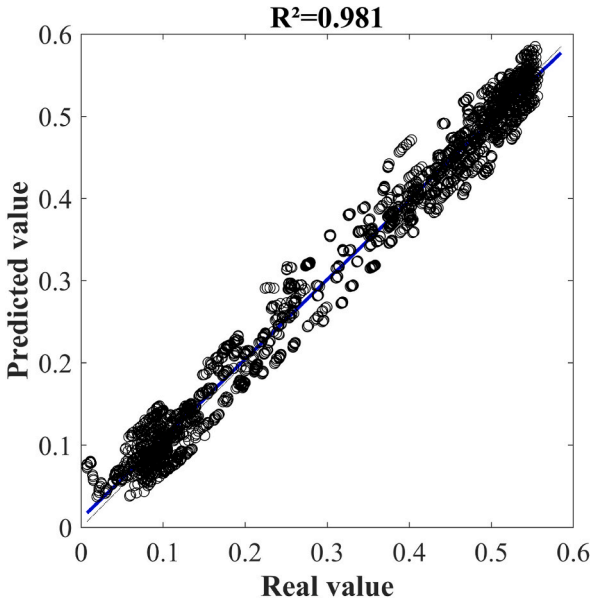

Fig. 7. Regression plot of predicted and true values on the test set.

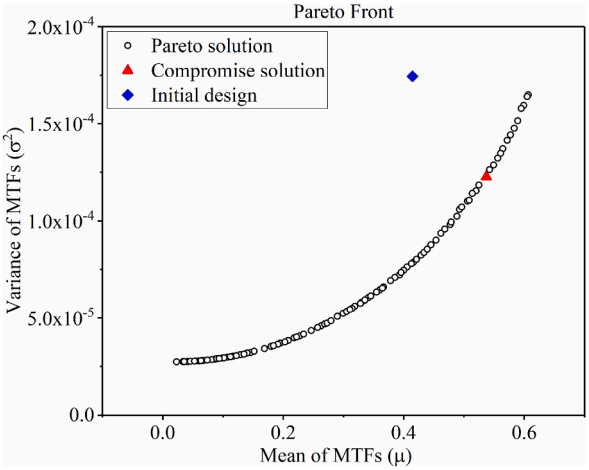

Fig. 8. Pareto front of NSGA-II

Table 3
Performance indicators of different optimization schemes.

Optimization Scheme	Predicted value		Simulated value		Relative error(%)	
	μ	σ^2	μ	σ^2	μ	σ^2
Optimization scheme targeting the mean of MTFs	0.60692	1.649×10^{-4}	0.55416	1.594×10^{-4}	9.5	3.5
Compromise solution	0.537	1.228×10^{-4}	0.53866	1.241×10^{-4}	−0.3	−1.0
Optimization scheme targeting the variance of MTFs	0.02324	0.274×10^{-4}	0.02512	0.298×10^{-4}	−7.5	−8

Table 4
Decision variables of different design schemes.

Design Scheme	X_1	X_2	X_3	X_4	X_5	X_6	X_7
Initial design scheme	1000	500	750	0.7	0.7	0.7	0.1
Optimal design scheme	482.57	1637	373.43	0.859	0.688	0.871	0.865
Design Scheme	X_8	X_9	X_{10}	X_{11}	X_{12}	X_{13}	X_{14}
Initial design scheme	0.5	0.8	0.5	0.1	0.1	0.7	0.1
Optimal design scheme	0.177	0.249	0.376	0.301	0.895	0.893	0.831
Design Scheme	X_{15}	X_{16}	X_{17}	X_{18}	X_{19}	X_{20}	X_{21}
Initial design scheme	47.3	44.35	28.8	33.8	19.3	0.1	0.16
Optimal design scheme	37.9	35.29	91.5	56.7	32.89	0.05	0.19

Table 5 lists the means and variances of the MTFs at the Nyquist frequency for the 12 fields of view of the SORS for the two TCS design schemes. As shown in the simulated values in Table 5, the mean of the MTFs based on the optimal design scheme of TCS increased by 0.13793, and the optical performance of the SORS was improved by 34.4%. Simultaneously, the variance of the MTFs based on the optimal design scheme of TCS reduced by 0.565×10^{-4}, and the differences in the optical performance of different fields of view of the SORS reduced by 31.3%. The results showed that the comprehensive optical performance of the SORS could be significantly improved by adopting the optimal design scheme of TCS.

5. Conclusion

In this paper, a multidisciplinary optimization method for the TCS of a SORS was proposed. Based on the surrogate model, a mapping relationship between the design parameters of the TCS and the optical performance of the SORS was established. Considering the mean and variance of the MTFs of 12 fields of view of the SORS at the Nyquist frequency as the objectives, the multi-objective optimization method NSGA-II was used to obtain a series of Pareto solutions. Some important conclusions are as follows:

1) The surrogate model established using PSO-BPNN could accurately predict the optical performance of the SORS, thus saving the time cost of simulation based on opto-mechanical-thermal integration.

Table 5
Performance indicators of different design schemes.

Design Scheme	Predicted value		Simulated value	
	μ	σ^2	μ	σ^2
Initial design scheme	0.41457	1.744×10^{-4}	0.40073	1.806×10^{-4}
Optimal design scheme	0.537	1.228×10^{-4}	0.53866	1.241×10^{-4}
Amount of change(%)	29.5	−29.6	34.4	−31.3

2) The optimization scheme targeting the mean of the MTFs exhibited the largest μ (0.60692), but also the largest variance σ^2 (1.649×10^{-4}). The optimization scheme targeting the variance of the MTFs obtained the smallest σ^2 (0.274×10^{-4}), but also the smallest mean μ (0.02324). The optimization scheme balanced these two objectives.
3) Based on the optimal design scheme obtained using NSGA-II, the SORS showed better comprehensive optical performance. Compared with the initial design scheme, the optical performance of the SORS was improved by 34.4%, and the differences in optical performance of different fields of view was reduced by 31.3%.
4) The optimal parameters of the TCS could be determined based on both the opto-mechanical-thermal integration analysis and NSGA-II method, thus guiding thermal engineers to better select design parameters during the design process of TCS of SORS.

Author statement

Zhipeng Yuan: Conceptualization, Methodology, Validation, Formal analysis, Investigation, Writing-original draft. **Liheng Chen:** Methodology, Resources, Writing-review & editing, Supervision, Project administration, Funding acquisition. **Hasiaoqier Han:** Writing-review & editing, Visualization. **Limin Ren:** Formal analysis, Writing-review & editing, Visualization. **Shuai Liu:** Validation, Formal analysis, Visualization. **Renxin Wang:** Formal analysis, Visualization.

Declaration of competing interest

The authors declare that they have no known competing financial interests or personal relationships that could have appeared to influence the work reported in this paper.

Data availability

Data will be made available on request.

Acknowledgments

This work was supported by The National Key Research and Development Program of China (No.2021YFB3901000, 2021YFB3901004).

References

[1] J.H. Li, J.Q. Wang, E. Lu, et al., Thermal-optical Analysis and Thermal Design of a Space Telescope, vol. 736, AIAA 38th Aerospace Sciences Meeting and Exhibit, 2000, https://doi.org/10.2514/6.2000-736.
[2] E.K.J. Jaekel, W. Erne, G. Soulat, The thermal control system of the faint object camera (FOC), AIAA 15th Thermophysics Conference 1501 (1980), https://doi.org/10.2514/6.1980-1501.
[3] H.X. Zhang, G.L. Huang, J. Yang, Thermal design and analysis of a hard X-ray modulation telescope, J. Thermophys. Heat Tran. 22 (2008) 528–530, https://doi.org/10.2514/1.34467.
[4] B.M. Shaughnessy, P. Eccleston, Thermal Design of the Mid-infrared Instrument (MIRI) for the James Webb Space Telescope, SAE Technical Paper Series, 2008, https://doi.org/10.4271/2008-01-2069.
[5] G. Morgante, L. Terenzi, P. Eccleston, et al., Thermal architecture of the exoplanet characterisation observatory payload, space telescope and instrumentation 2014: optical, infrared, and millimeter wave, SPIEL 9143 (2014) 1030–1042, https://doi.org/10.1117/12.2056800.
[6] G. Morgante, L. Terenzi, P. Eccleston, et al., Thermal control system of the exoplanet characterisation observatory payload: design and predictions, Exp. Astron. 40 (2015) 771–800, https://doi.org/10.1007/s10686-015-9469-7.
[7] S.J. Li, L.H. Chen, Y.T. Yang, Thermal design and test verification of the solar X-ray and extreme ultraviolet imager, Optik 203 (2020), https://doi.org/10.1016/j.ijleo.2019.164017.
[8] S.J. Li, L.H. Chen, Y.H. Wu, Thermal design of detector for the solar X-ray and extreme ultraviolet imager, J. Thermophys. Heat Tran. 33 (2) (2019) 285–291, https://doi.org/10.2514/1.T5423.
[9] E. Escobar, M. Diaz, J.C. Zagal, Evolutionary design of a satellite thermal control system: real experiments for a CubeSat mission, Appl. Therm. Eng. 105 (2016) 490–500, https://doi.org/10.1016/j.applthermaleng.2016.03.024.
[10] Y.T. Yang, L.H. Chen, Y. Xiong, et al., Global sensitivity analysis based on BP neural network for thermal design parameters, J. Thermophys. Heat Tran. 35 (2021) 187–199, https://doi.org/10.2514/1.T5955.
[11] G.P. Zhang, H. Zhao, Y.H. Chen, et al., Optimization thermal design method for space cameras based on thermo-optical analysis and Taguchi method, Opt. Eng. 59 (7) (2020), 075101, https://doi.org/10.1117/1.OE.59.7.075101.
[12] G. Cataldo, M.B. Niedner, D.J. Fixsen, et al., Model-based thermal system design optimization for the James Webb space telescope, J. Astronomical Telesc. Instrum. Syst. 3 (4) (2017), 044002, https://doi.org/10.1117/1.JATIS.3.4.044002.
[13] R.L. Galski, F.L. De Sousa, F.M. Ramos, et al., Spacecraft thermal design with the generalized extremal optimization algorithm, Inverse Problem. Sci. Eng. 15 (1) (2007) 61–75, https://doi.org/10.1080/17415970600573924.
[14] I. Muraoka, R.L. Galski, F.L. De Sousa, et al., Stochastic spacecraft thermal design optimization with low computational cost, J. Spacecraft Rockets 43 (6) (2006) 1248–1257, https://doi.org/10.2514/1.20066.

[15] R. Gracey, A. Bartoszyk, E. Cofie, et al., Structural, thermal, and optical performance (STOP) modeling and results for the James Webb space telescope integrated science instrument module, modeling, systems engineering, and project management for astronomy VII, SPIEL 9911 (2016) 522–541, https://doi.org/10.1117/12.2233641.
[16] M. Borden, D. Lewis, H. Ochoa, et al., Thermal, structural, and optical analysis of a balloon-based imaging system, Publ. Astron. Soc. Pac. 129 (973) (2017), 035001, https://doi.org/10.1088/1538-3873/129/973/035001.
[17] S.J. Scola, J.F. Osmundsen, L.S. Murchison, et al., Structural-Thermal-Optical Performance (STOP) Model Development and Analysis of a Field-Widened Michelson Interferometer, Novel Optical Systems Design and Optimization XVII, vol. 9193, SPIE, 2014, pp. 133–147, https://doi.org/10.1117/12.2061041.
[18] N. Sawruk, M. Albert, S. Litvinovitch, et al., Structural Thermal Optical (STOP) Analysis of the Space-Qualified Laser Transmitter for the ICESat-2 Mission, CLEO: Applications and Technology, Optica Publishing Group, 2013, https://doi.org/10.1364/CLEO_AT.2013.AF1H.3.
[19] C.B. McMenamin, Application of Bayesian-Based Uncertainty and Global Sensitivity Analyses to Spacecraft Thermal Design, Massachusetts Institute of Technology, 2016. http://hdl.handle.net/1721.1/105622.
[20] K. Deb, A. Pratap, S. Agarwal, et al., A fast and elitist multiobjective genetic algorithm: NSGA-II, IEEE Trans. Evol. Comput. 6 (2) (2002) 182–197, https://doi.org/10.1109/4235.996017.
[21] H.Z. Yang, J. Wen, S.M. Wang, et al., Thermal design and optimization of plate-fin heat exchangers based global sensitivity analysis and NSGA-II, Appl. Therm. Eng. 136 (2018) 444–453, https://doi.org/10.1016/j.applthermaleng.2018.03.035.
[22] R. Arora, S.C. Kaushik, R. Arora, Multi-objective and multi-parameter optimization of two-stage thermoelectric generator in electrically series and parallel configurations through NSGA-II, Energy 91 (2015) 242–254, https://doi.org/10.1016/j.energy.2015.08.044.
[23] L.C. Zhang, M.Y. Lv, W.Y. Zhu, et al., Mission-based multidisciplinary optimization of solar-powered hybrid airship, Energy Convers. Manag. 185 (2019) 44–54, https://doi.org/10.1016/j.enconman.2019.01.098.
[24] U. Lee, S. Park, I. Lee, Robust design optimization (RDO) of thermoelectric generator system using non-dominated sorting genetic algorithm II (NSGA-II), Energy 196 (2020), 117090, https://doi.org/10.1016/j.energy.2020.117090.
[25] C.L. Li, Y.L. Ding, C. Lin, et al., Optomechanical design and simulation of a cryogenic infrared spectrometer, Appl. Opt. 59 (2020) 4642–4649, https://doi.org/10.1364/AO.392621.
[26] Z.P. Yuan, X. Meng, C.L. Li, et al., Research on thermal design and thermal optical performance of space telescope based on multidisciplinary integration, J. Therm. Stresses 45 (2022) 401–414, https://doi.org/10.1080/01495739.2022.2049023.
[27] V. Lakshminarayanan, A. Fleck, Zernike polynomials: a guide, J. Mod. Opt. 58 (7) (2011) 545–561, https://doi.org/10.1080/09500340.2011.554896.
[28] J.T. Hwang, J.R.R.A. Martins, A fast-prediction surrogate model for large datasets, Aero. Sci. Technol. 75 (2018) 74–87, https://doi.org/10.1016/j.ast.2017.12.030.
[29] P. Jiang, Q. Zhou, X.Y. Shao, Surrogate Model Based Engineering Design and Optimization, Springer, Singapore, 2020, https://doi.org/10.1007/978-981-15-0731-1.
[30] S.W. Kim, J.A. Melby, N.C. Nadal-Caraballo, et al., A time-dependent surrogate model for storm surge prediction based on an artificial neural network using high-fidelity synthetic hurricane modeling, Nat. Hazards 76 (2015) 565–585, https://doi.org/10.1007/s11069-014-1508-6.
[31] J. Dong, W.W. Qin, J.J. Mo, Low-cost multi-objective optimization of multiparameter antenna structures based on the l1 optimization BPNN surrogate model, Electronics 8 (8) (2019) 839, https://doi.org/10.3390/electronics8080839.
[32] G.Z. Huang, B. Yan, Z.Y. Mou, et al., Surrogate model for torsional behavior of bundle conductors and its application, IEEE Trans. Power Deliv. 37 (1) (2021) 67–75, https://doi.org/10.1109/TPWRD.2021.3053341.
[33] J. Kennedy, R. Eberhart, Particle swarm optimization, proceedings of ICNN'95-international conference on neural networks, IEEE 4 (1995) 1942–1948, https://doi.org/10.1109/ICNN.1995.488968.
[34] J. Dong, Y.J. Li, M. Wang, Fast multi-objective antenna optimization based on RBF neural network surrogate model optimized by improved PSO algorithm, Appl. Sci. 9 (13) (2019) 2589, https://doi.org/10.3390/app9132589.
[35] P.Z. Cui, M.X. Yu, Z.Q. Liu, et al., Energy, exergy, and economic (3E) analyses and multi-objective optimization of a cascade absorption refrigeration system for low-grade waste heat recovery, Energy Convers. Manag. 184 (2019) 249–261, https://doi.org/10.1016/j.enconman.2019.01.047.